Deformation kinetics of a TRIP steel determined by in situ high-energy synchrotron X-ray diffraction

P. Barriobero-Vila [a, *], R. Jerez-Mesa [b], A. Guitar [c], O. Gavalda-Diaz [d], J. A. Travieso-Rodríguez [b], A. Stark [e], N. Schell [e], J. Llumà [f], G. Fargas [g], A. Mateo [g], J. J. Roa [g, *]

a) Institute of Materials Research, German Aerospace Center (DLR), Linder Höhe, 51147 Cologne, Germany

b) Department of Mechanical Engineering, Barcelona East School of Engineering (EEBE), Technical University of Catalonia-BarcelonaTech (UPC), 08019 Barcelona, Spain

c) Functional Materials, Department of Materials Science and Engineering, Saarland University, 66123 Saarbrücken, Germany

d) Department of Materials, Faculty of Engineering, Imperial College London, SW7 2AZ London, United Kingdom

e) Helmholtz-Zentrum Hereon, Max-Planck-Straße 1, 21502 Geesthacht, Germany

f) Department of Materials Science and Engineering, Barcelona East School of Engineering (EEBE), Technical University of Catalonia-BarcelonaTech (UPC), 08019 Barcelona, Spain

g) Center for Research in Structural Integrity, Reliability and Micromechanics of Materials (CIEFMA), Department of Materials Science and Engineering, Barcelona East School of Engineering (EEBE), Technical University of Catalonia-BarcelonaTech (UPC), 08019 Barcelona, Spain

* Corresponding authors:

pere.barrioberovila@dlr.de (P. Barriobero-Vila), joan.josep.roa@upc.edu (J. J. Roa)

Abstract

The microstructure design and the development of predictive approaches exploiting the transformation-induced plasticity (TRIP) effect require a keen understanding of the kinetics governing the strain-induced martensitic transformation. In this work, in situ high-energy synchrotron X-ray diffraction is applied to track the deformation kinetics of a commercial AISI 301LN metastable austenitic stainless steel in real-time. The kinetics obtained, providing the behaviour of the bulk material during room temperature tension up to a true strain of 0.3, unambiguously reveals the transformation sequence of ε and α′ martensite which is discussed with respect to the evolution of texture and slip. These results are enhanced with microstructure analysis including electron backscattered diffraction and transmission Kikuchi diffraction. The insights provided shed light on the role of ε during α′ transformation in metastable austenitic stainless steels and show that the latter is triggered by the general activation of slip.

Keywords: TRIP-aided steels, stainless steels, deformation kinetics, in situ high-energy synchrotron X-ray diffraction

1. Introduction

Metastable austenitic stainless steels are used in multiple engineering applications including the automotive and aerospace sectors owing to their corrosion resistance, strength and good formability [1, 2]. The martensitic transformation occurring in these materials allows adjusting their mechanical properties by tuning combinations of austenitic and transformed states associated with large ductility and strength, respectively. The strain-induced transformation of the face-centered cubic (fcc)

austenite (γ) to the body-centered cubic (bcc) α′ martensite (γ → α′) leads to outstanding work hardening as well as high plasticity [3]. During this process, transformation-induced plasticity (TRIP) provides significantly enhanced plasticity during the phase change [4, 5]. Also, a volume expansion of ~4 % occurs as a consequence of the transformation [6]. This process is accompanied by the formation of the hexagonal close-packed (hcp) ε-martensite, observed for instance in manganese and chromium-manganese steels [7].

The control of the chemical composition, stacking fault energy (SFE) and processing parameters such as stress, strain rate and temperature, is highly important to determine the generated fractions of γ and α′ i.e. the resulting mechanical performance of steels [8, 9]. This requires a keen understanding of the deformation kinetics driving these processes which contribute to the development of predictive approaches. The transformation sequence γ → ε → α′ has been reported for austenitic stainless steels deformed by tension and rolling [10–13]. On the other hand, the direct γ → α′ transformation was proposed in previous investigations denoting an important role of dislocation activity in this process [14–16]. For austenitic stainless steels with low stacking fault energy (SFE) (< 18 mJ/m^2) it is assumed that the formation of ε is a favoured deformation mechanism. The SFE depends on chemical composition and temperature. Along with experimental determination of values for SFE, another problem for metastable austenitic steels is the accurate description of deformation mechanisms depending on SFE [5].

According to the Olson-Cohen mechanism [17], the intersections of shear bands are effective sites for α′ nucleation. They can contain ε martensite, mechanical twins, dense

stacking fault bundles and planar slip bands [17, 18]. Moreover, the growth of α′ is stated to occur by repeated nucleation of embryos and coalescence.

Most of the studies providing understanding of the phase transformations in TRIP steels are based on local analyses involving single grains and limited phase arrangements barely representing the behaviour of the bulk material [19–22]. Although important insights have been gained in these works from local analysis and post-mortem conditions after deformation, the study of the continuous phase evolution within the bulk has received less attention. This limits the provision of bulk information about the kinetics of phase transformation, texture or the deformation mechanisms operating in the representative material volume. In this regard, in situ X-ray diffraction is a potential technique to overcome these drawbacks [23–27].

In situ high-energy synchrotron X-ray diffraction (HEXRD) allows determining the deformation kinetics of engineering alloys with a time resolution under one second. The high penetration of this technique, combined with the use of 2D detectors permits a fast acquisition of entire Debye-Scherrer rings of the bulk in a single beam shot [28, 29]. This technique is non-destructive and well suited to investigate processes during thermal or mechanical loading of steels [30–33]. Compared to previous bulk analysis to study the TRIP kinetics, the present work aims at combining in situ HEXRD with complementary techniques not only to obtain insights from the macrostructure evolution, but also to provide a comprehensive characterization at relevant length scales.

In the present work, the deformation kinetics of a commercial AISI 301LN TRIP metastable austenitic stainless steel is studied using in-situ HEXRD during tensile deformation up to a true strain of 0.3. This alloy is used in transport applications such as

components of the vehicle chassis and railroad cars. The investigations are complemented by microstructure analysis including electron backscattered diffraction (EBSD) as well as examination of thin-foils by transmission Kikuchi diffraction (TKD). The formation sequence of α' and ε is unambiguously revealed as a function of strain. Initially, plastic deformation takes place via the formation of stacking faults and ε. As the strain increases, formation of $\gamma \rightarrow \alpha'$ leads to an increase of the strain hardening rate. The results obtained show that the latter transformation is triggered by a general activation of slip and support a major contribution of a direct $\gamma \rightarrow \alpha'$ path since no significant two-stage $\gamma \rightarrow \varepsilon \rightarrow \alpha'$ transformation involving $\varepsilon \rightarrow \alpha'$ is observed.

2. Experimental

2.1. Material

The investigated material is a commercial AISI 301LN (EN 1.4318) metastable austenitic stainless steel supplied by Outokumpu as 1.6 mm thick sheets. The as-received condition is obtained after annealing at 1100 °C for 1 hour and presents a fully homogeneous austenitic microstructure prior deformation. This can be observed in the analogous microstructures with equiaxed γ grains obtained from the sample regions center and surface (Fig. S1 of supplementary material). The chemical composition is given in **Table 1**. Further information of this material is available in [34]. The as-received material presents an austenitic microstructure (**Fig. 1a**). Accordingly, the complete Debye-Scherrer rings obtained by HEXRD are associated with γ (**Fig. 1d**). Scarce martensitic α' plates may be present in the as-received microstructure as indicated in **Fig. 1a**.

Specimens of the as-received material were prepared by laser cutting for room temperature (RT) tensile testing in the rolling (RD) and transversal (TD) directions. The sample's geometry employed is given in **Fig. 1e** (*thickness*= 1.6 mm). As a consequence of the fairly isotropic microstructure of the as-received material, RD and TD present an analogous evolution of the stress-strain and strain-hardening rate curves (**Fig. 1b**). When comparing both directions, the texture analysis obtained by HEXRD shows non-remarkable preferential orientations of γ. Thus, only the RD condition will be considered onwards for further investigations. Additional details of the tensile experiments are provided in the next **section 2.2**.

Table 1. Composition of the studied 301LN stainless steel.

Element	C	Cr	Ni	Mn	Si	Mo	N	Fe
wt.%	0.02	17.48	7.03	1.23	0.45	0.12	0.12	Balance

2.2. In situ high-energy synchrotron X-ray diffraction

In situ high-energy synchrotron X-ray diffraction (HEXRD) was carried out at the P07-HEMS beamline of PETRA III, Deutsches Elektronen-Synchrotron (DESY) [35]. The experimental parameters are summarized in **Table 2**. RT tensile tests were performed using a modified dilatometer Bähr 805A/D equipped with a deformation unit [36]. Flat samples of 1.6 mm in thickness and the geometry shown in **Fig. 1e** were deformed at a strain rate of 0.001 s^{-1}. The strain is obtained by an extensometer linked to a rod measuring the displacement of the gauge volume. An illustrative picture of the experimental setup is presented in **Fig. 1e**. The incident X-ray beam is positioned at the centre of the samples during deformation. Image sequences of complete Debye-Scherrer

rings from the bulk of the samples were recorded in transmission mode (*thickness*=1.6 mm) during uniaxial tension using an image-plate detector (*sample's gauge volume*= $1\times1\times1.6$ mm^3). **Fig. 1d** shows representative examples of the acquired images. The instrumental parameters of the HEXRD setup were obtained using a LaB_6 powder standard.

Table 2. In situ high-energy synchrotron X-ray diffraction performed at the beamline P07-PETRA III: experimental parameters.

Energy [keV]	Wavelength [Å]	Slit-aperture size [mm^2]	Sample-detector distance [mm]	Acquisition time [s/image]	Detector
100	0.124	1×1	1593.2	1	PerkinElmer XRD 1621

2.3. Data processing

Qualitative analysis of the evolution of the diffraction images during uniaxial tension was carried out by converting the Debye-Scherrer rings into Cartesian coordinates (azimuthal angle-ψ, 2θ). Subsequently, the following processing was carried out using the software ImageJ [37]: a) projection of the sum intensity of Bragg reflections on the 2θ axis, and b) projection of the sum intensity of Bragg reflections on the azimuthal axis.

Quantitative phase analysis of the entire Debye-Scherrer rings was carried out using the Rietveld method as implemented in the software MAUD [38]. For this procedure, an extended Williams-Imhof-Matthies-Vinel algorithm (E-WIMV) integrated in MAUD

was used for considering the texture evolution during deformation. A satisfactory quality factor of R_w< 10 % was obtained. This software was also used for peak profile analysis describing the size of coherently diffracting domains and the local lattice strains produced by microstructure defects [39]. In this regard, the calculation of crystallize size (coherently diffracting domains) and root mean square microstrain ($<\varepsilon^2>^{1/2}$) was evaluated using the size-strain Popa model [40]. The instrumental broadening was described by the Cagliotti PV model implemented in MAUD. Its parameters were obtained from a LaB_6 powder standard.

The lattice strains were calculated in the tensile direction (T) from the 2θ variations of individual {hkl} reflections comprised within azimuthal sections of 10 °. A schematic diagram of this methodology is provided in [28]. The calculation was performed according to:

$$\varepsilon_i = \frac{d_i - d_0}{d_0} \qquad (1)$$

where, ε_i and d_i are the strain and the interplanar *d-spacing* of the lattice at a deformation step *i*, respectively; d_0 is the d-spacing obtained for the initial condition. The Olson and Cohen model [41] was applied to obtain the volume fraction of shear bands in austenite during deformation. For that, the volume fraction of α′ martensite obtained by Rietveld analysis as a function of strain was initially fit to obtain the parameters α and β:

$$f^{\alpha'} = 1 - \exp\{-\beta[1 - \exp(-\alpha\varepsilon)]^n\} \qquad (2)$$

where, α represents the rate of shear-band formation, β is proportional to the probability that a shear-band intersection will generate a martensitic embryo, ε is the plastic strain, and the exponent *n* describes the rate of the formation of the shear band intersections, which is frequently a constant of 4.5 [41]. The values α= 8.11 and β= 0.62 were derived

from the calculation (R^2 = 0.99). After this procedure, the volume fraction of shear bands in austenite during deformation is calculated using:

$$f^{sb} = 1 - \exp(-\alpha\varepsilon) \quad (3)$$

where, f^{sb} is the volume fraction of shear bands in austenite related to the plastic strain ε, and α represents the rate of shear-band formation. The model assumes that the formation of martensitic embryos is directly proportional to the number of shear-band intersections.

2.4. Microstructure characterization

2D analysis of the microstructure prior and after uniaxial RT tension was performed using scanning electron microscopy (SEM) and electron backscatter diffraction (EBSD). For SEM investigations, a Zeiss Neon 40 field emission scanning electron microscopy (FESEM) was employed at 5 kV. On the other hand, EBSD analysis were carried out for an area of 540×375 μm^2 using a Zeiss Ultra 55 field FESEM operated at 10kV. An Oxford Nordlys II EBSD detection system was employed in combination with the acquisition software AZtec. The data processing was carried out using the Channel 5 software. The beam step-size, working distance and sample-tilt angle used are 0.25 μm, 9.5 mm and 70 °, respectively. The specimens were electropolished during 25 s at 16 V and -20 °C using an electrolyte consisting of perchloric acid (11 %), ethanol (18 %) and methanol (71 %). This method was effective in avoiding the presence of stress induced martensite during metallographic preparation.

In addition, thin-foils were prepared for transmission Kikuchi diffraction (TKD) by employing a dual-beam FE-SEM Helios nanolab 600 FEI. The samples were prepared according the procedure described in [42], avoiding the final thinning of the sample. A

final milling step at low voltage (2 kV) was performed in order to minimize Ga^+ implantation. During TKD, an EDAX TSL OIM data collection system was used in combination with the following parameters: 20 keV, 22 nA and step size of 30 nm. The density of geometrically necessary dislocations (GNDs) is provided according to the methodology proposed in [43]. This algorithm considers both types of dislocations: edge and screw.

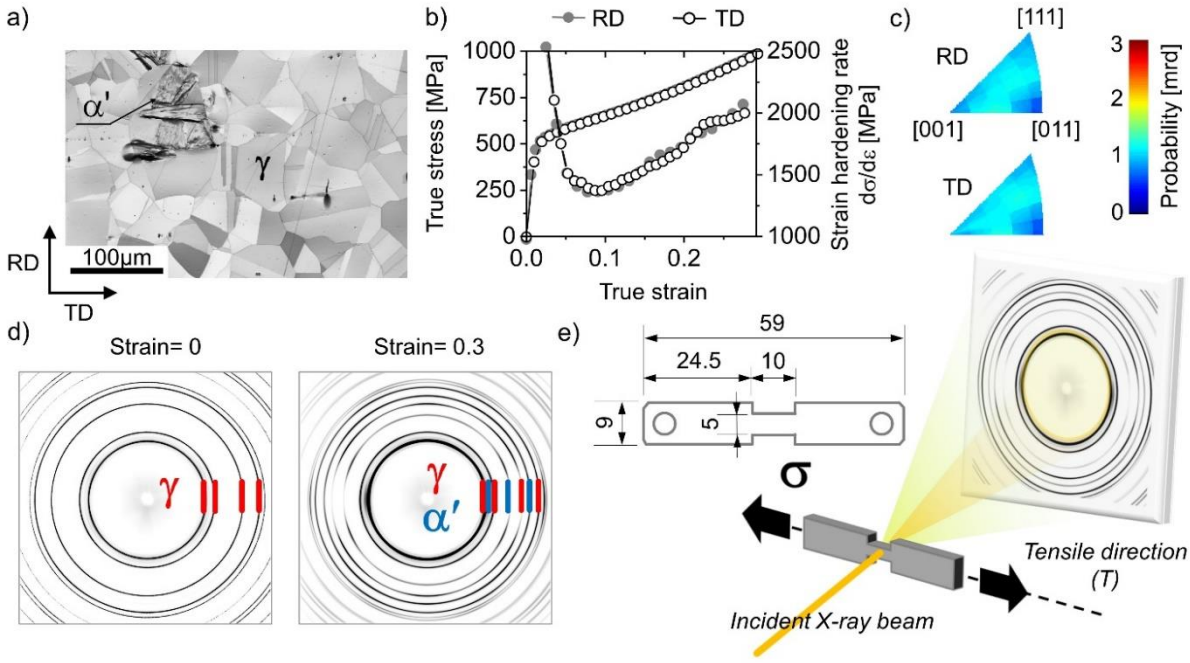

Fig. 1. a) Scanning electron microscopy of the studied 301LN metastable austenitic stainless steel prior deformation. **b)** Curves for the evolution of the true stress-strain and strain-hardening rate obtained during uniaxial tension of RD and TD specimens. **c)** Inverse pole figures (IPF) from the bulk of RD and TD specimens obtained in the tensile direction (T) by high-energy synchrotron X-ray diffraction, HEXRD (*gauge volume*= 1×1×1.6 mm^3). **d)** HEXRD images obtained prior deformation (strain = 0) and during deformation up to strain= 0.3. The Debye-Scherrer rings of γ and γ+α′ phases are visible in the former and latter conditions, respectively. **e)** Schematic drawing of the

experimental setup used for in situ synchrotron HEXRD during uniaxial tension at room temperature. The dimensions of the tensile specimens are given in mm (*sample thickness*=1.6 mm).

3. Results and discussion

3.1. Deformation kinetics

Fig. 2 shows the evolution of {hkl} reflections of γ, α′ and ε during RT uniaxial tension. The colour-coded plot provides a qualitative analysis of the phase evolution. At strain= 0, the following reflections of ε and γ are present: {100}ε, {111}γ–{002}ε, {101}ε, {200}γ, {220}γ–{110}ε, {311}γ–{112}ε and {222}γ. During deformation up to strain ~0.075, {110}α′, {200}α′ and {211}α′ reflections start to form indicating the onset of the γ → α′ transformation. Thereafter, the intensity of these reflections increases with strain up to the maximum applied deformation (strain= 0.3). At the same time, a continuous increase of the strain hardening rate (dσ/dε) takes place from the γ → α′ onset (see left-hand side of **Fig. 2**). This effect agrees with the significant increase in the work-hardening rate reported for the strain-induced α′ martensite transformation [44].

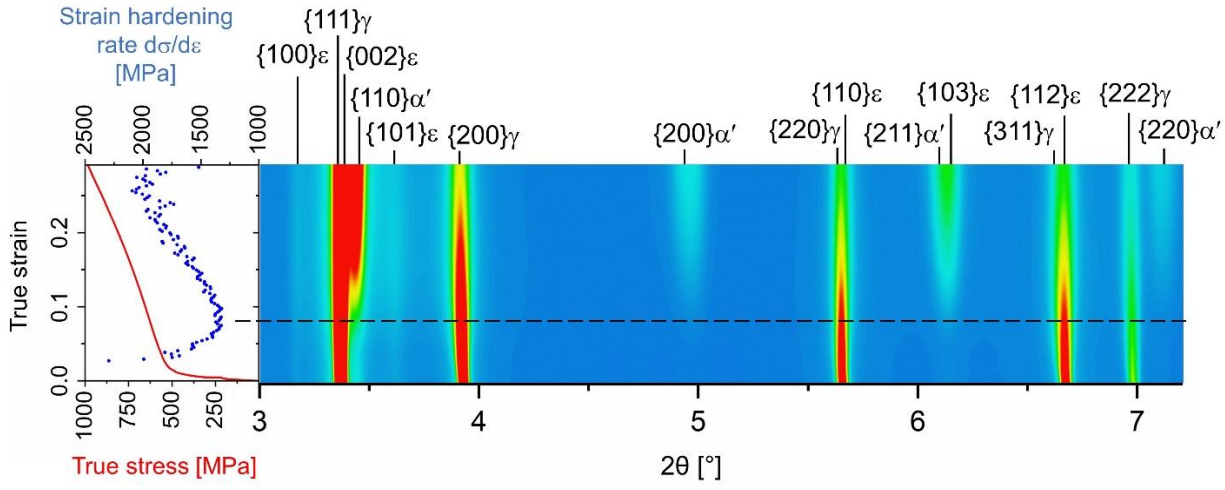

Fig. 2. Colour-coded 2D plot of the evolution of {hkl} reflections of γ, α′ and ε phases during uniaxial tension of the 301LN alloy at room temperature. A representative 2θ range of 3–7.2º is presented. The left-hand diagram shows the evolution of the true stress-strain and of the strain hardening rate (dσ/dε) in red and blue, respectively.

Fig. 3a, **b** and **c** show the complete Debye–Scherrer rings converted into Cartesian coordinates obtained during deformation up to a true strain of 0, 0.05 and 0.1, respectively. This figure shows that the γ → α′ transformation coexists with the presence of ε. Initially, reflections of γ and ε are present (**Fig. 3a**). During deformation up to strain= 0.05 (**Fig. 3b**), the {100}, {101} and {103} reflections of ε increase their intensity. As the deformation progresses up to 0.1 (**Fig. 3c**), the reflections {200}, {211} and {220} of α′ start to form. This is also accompanied by an increase in intensity of {100}ε and {101}ε. However, it is important to note that the onset of the γ → α′ transformation is given by the quantitative evolution of phase volume fractions shown in Fig. 4a.

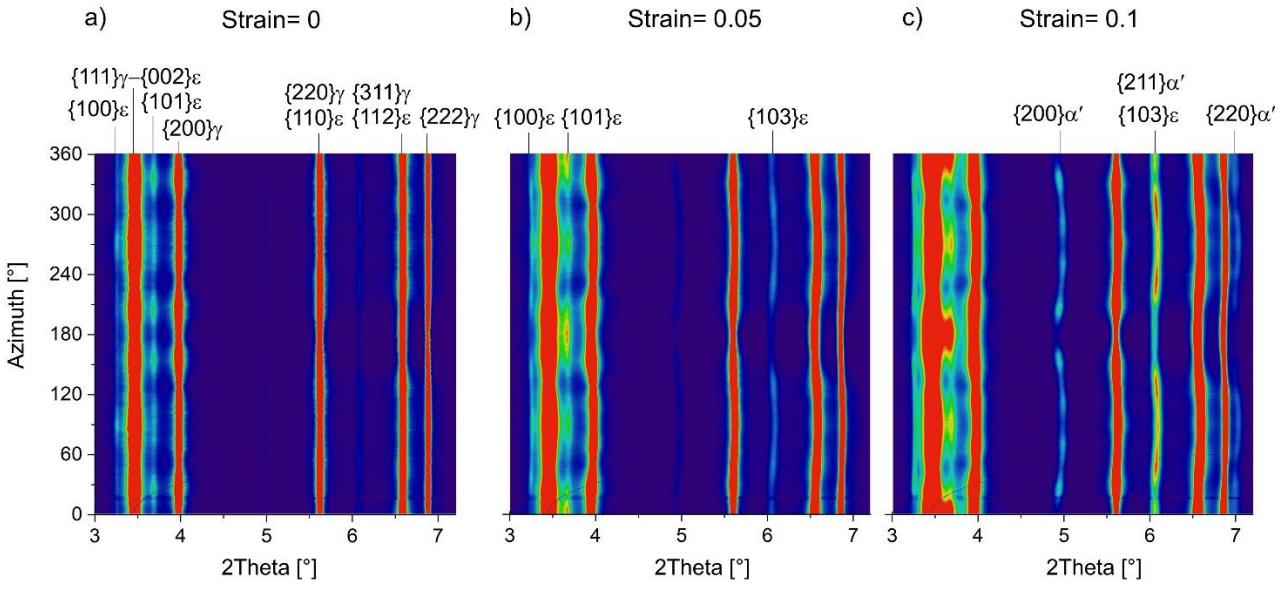

Fig. 3. Complete Debye–Scherrer rings converted into Cartesian coordinates obtained for the 301LN alloy during tensile deformation: **a)** initial condition (true strain= 0), **b)** true strain= 0.05 and **c)** true strain= 0.1. For simplicity, b) and c) show the transforming reflections. The rest of {hkl} lines are shown in a).

The evolution of phase volume fractions obtained by Rietveld analysis for γ, ε and α′ is presented as a function of strain in **Fig. 4a**. During deformation up to 0.075, ε increases up to ~0.22. Also, a simultaneous decrease of γ down to ~0.74 takes place. At higher deformation, the volume fraction of ε remains relatively constant. α′ starts to form at strain 0.075, increasing up to 0.33 at the maximum applied strain of 0.3. At the same time, γ presents a linear decrease down to 0.40. The results obtained reveal that the increase of work hardening observed in **Fig. 2** is a consequence of the formation of α′. In the investigated steel, the formation of ε is plausible since the SFE of this material (12–15 mJ/m^2 [45]) remains below the upper limit established for the formation of this phase (~18 mJ/m^2) [5]. It is important to note that a limited detection of fine ε particles and small volume fractions of this phase may be expected when using X-ray diffraction. Thus, it is important considering this factor when discussing the phase transformations involved during deformation.

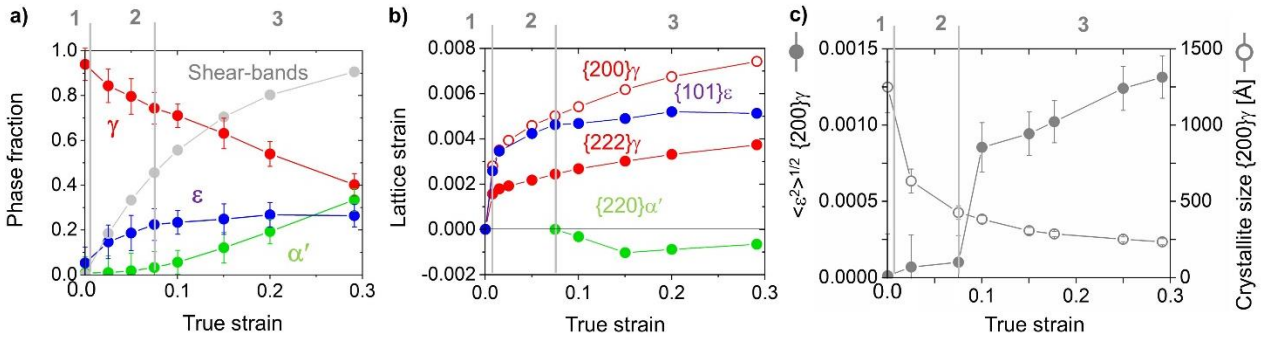

Fig. 4. Evolution of **a)** phase volume fractions, **b)** lattice strains {200}γ, {101}ε, {222}γ and {220}α′ in the tensile direction (errors included within the symbols), **c)** root mean square microstrain $<\varepsilon^2>^{1/2}$ and crystallite size of {200}γ as a function of true strain during uniaxial tension of 301LN.

Fig. 4a shows that ε formation is favoured at low strains up to 0.075. Below this onset, this phase constitutes a significant fraction of the shear bands estimated using the Olson and Cohen model, since ε is a result of shear-band formation via regular overlapping of staking faults [17, 45]. However, this contribution becomes less relevant at strains higher than this onset. The shear-band mechanism driving the formation of this phase is also reflected in the asymptotic trend presented by the volume fraction evolution of both shear-bands and ε formation. The kinetics obtained in **Fig. 4a** are comparable with those reported for a metastable austenitic 16Cr–7Mn–xNi steel [27] and an analogous 301LN alloy [46]. In the latter, the γ → ε transformation starts close to zero strain and shows a parabolic transformation behaviour until reaching a constant amount of ε; in addition to a linear increase of α′.

Fig. 4b displays the evolution of the lattice strains in T for {200}γ, {101}ε, {222}γ and {220}α′ as a function of true strain. Firstly, those of γ and ε present a steep increase up to the yield point at true stress and true strain ~415 MPa and ~0.008, respectively. This value is obtained by considering the maximum of the second derivative of the stress strain curve as explained in [47]. Three different stages are visible. The stage 1 of deformation (strain 0–0.008) corresponding to the elastic regime is observed as an initial linear increase of lattice strains. On the other hand, during stage 2 (**Fig. 4b**), the lattice strains of γ and ε undergo a continuous increase up to strain 0.075. As observed

in **Fig. 4a**, this period (strain ~0.008–0.075) corresponds to ε formation. Thereafter, the γ → α′ transformation occurs between strains 0.075-0.3 in stage 3 (see **Fig. 4a**). Here, the lattice strain {101}ε undergoes a detachment from linearity, remaining relatively constant up to the end of deformation (**Fig. 4b**). At the same time, {200} and {222} of γ undergo a slight continuous increase, while the {220}α′ reflections forming during the transformation pointed in **Fig. 3c** remain in a compressive state.

The stress state of duplex stainless steels after solution-treatment and subsequent quenching consists of the ferritic α and γ in compression and tension, respectively, owing to the difference in thermal expansion between phases [48]. However, the stress behaviour of both bcc and fcc phases under loading requires further understanding. The strain-induced γ → α′ transformation occurring in austenitic stainless steels is associated with a shape change, volume expansion and a transformation strain. According to the crystallographic theory, the transformation is accomplished by the Bain distortion and a shear deformation at the interface between γ and α′ which can occur by slip or twinning [6]. Owing to the different elastic properties of γ and α′, the martensite formation has been associated with the presence of residual stresses [48]. During deformation, the mismatch between both phases leads to strain and stress partitioning [49].

Fig. 4c shows the evolution of the root mean square microstrain $<\varepsilon^2>^{1/2}$ and of the crystallite size of {200}γ during tensile deformation. This represents a single reflection not influenced by neighbour intensities which could lead to a biased interpretation of the results. In stage 2, a significant decrease of the crystallite size takes place. During plastic deformation of fcc metals, the crystallite size is affected by the accumulation of stacking faults and the decrease of this parameter is a result of the reduction of the

coherently diffracting domains [50, 39]. This effect correlates well with the mechanism of ε formation taking place during this deformation stage (**Fig. 4a**): namely the stacking fault activity in γ promoting ε formation when the ordering of dense stacking faults takes place by regular overlapping on every second {111}γ plane [45]. On the other hand, stacking fault bundles regarded as faulted austenite form if this overlapping is irregular [45].

The evolution of the root mean square microstrain shown in **Fig. 4c** allows analysing the development of the dislocation density in γ during plastic deformation owing to the proportionality between these variables [27, 51]. The low microstrain during stage 2 denotes that deformation is dominated by stacking fault formation and the ε transformation. The latter being visible in **Fig. 4a**. However, further tensile deformation from the onset of α′ transformation (strain 0.075), leads to a sudden increase of the microstrain up to strain 0.1. Thereafter, the microstrain increases with a lower rate of change during the γ → α′ progression. The sudden increase observed in **Fig. 4c** indicates an accelerated generation of dislocations in γ at the beginning of stage 3 which can be correlated with the general activation of slip pointed in **Fig. 5**.

Fig. 5 shows the evolution of {200}γ Bragg reflections during uniaxial tension. At the beginning of the deformation, the dispersed lines along the azimuth represent grains oriented in arbitrary directions. Thereafter, deformation between strain 0.075–0.2 leads to the formation of texture poles and slip-driven grain rotation (see arrows). These effects point to a general activation of slip in γ during stage 3. Grain rotation is represented by a gradual evolution of intensity along the azimuth moving towards preferred orientations (see arrows). **Fig. 5b** shows a detailed intensity evolution related to particular grains from the selected region in **Fig. 5a**. It can be observed that the

activation of slip leads to cone-like broadening of original γ reflections indicating a continuous activation of dislocations creating angular distortions, and the consequent formation of subgrains (S) indicated by arrows [28, 52]. This is accompanied by grain rotation (R). The general activation of slip correlates well with the sudden increase of microstrain seen at the beginning of stage 3 (**Fig. 4c**). Also, this onset is concurrent with that of α′ formation (**Fig. 4b**).

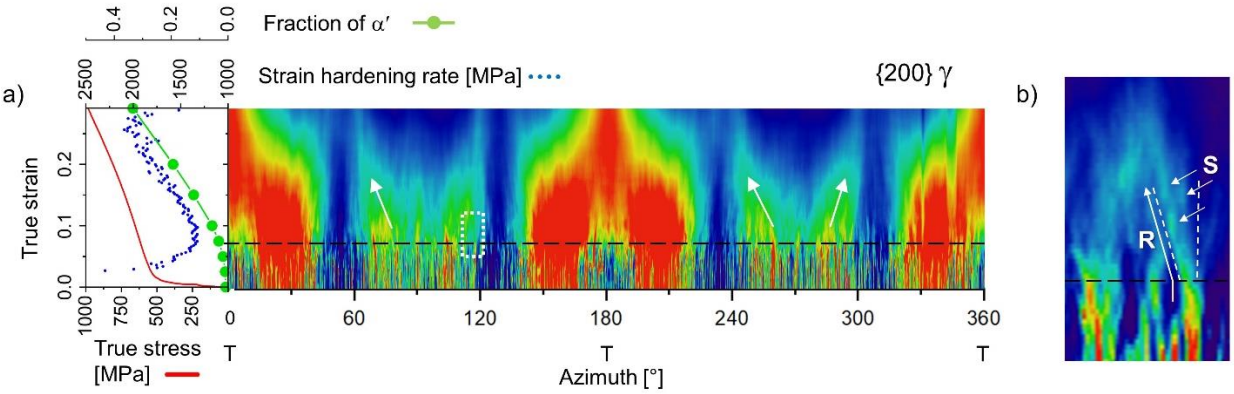

Fig. 5. a) Colour-coded 2D plot of the evolution of {200}γ Bragg reflections for the Azimuthal range 0–360° during uniaxial tension at room temperature. The tensile direction, T, corresponds to the azimuth angles 0/360° and 180°. **b)** Inset of the rectangular selected region in a).

The texture poles observed in **Fig. 5** between the strain ranges 0.075–0.2 and 0.2–0.3 are associated with the corresponding ⟨111⟩∥T and ⟨100⟩∥T preferential orientations developed in γ during tensile deformation. This can be observed in **Fig. 6**, showing the texture evolution of γ, α′ and ε from the bulk alloy obtained by in situ HEXRD. As a consequence of {111}⟨110⟩ slip, well known to take place in fcc metals, the activation of this mechanism in γ results in the orientation of initially randomly oriented grains towards ⟨111⟩∥T (**Fig. 6a**). As the deformation increases (**Fig. 6b** and **c**), this effect

becomes more pronounced. Together with the development of this main texture component, weaker ⟨100⟩∥T preferential orientations form in γ between strain 0.2–0.3 (see **Fig. 5** and **Fig. 6c**). The double fibre texture obtained agrees with the results reported for uniaxial tensile deformation of austenitic steels presenting weak initial textures [53]. In stage 3, slip in γ is accompanied by α′ formation, the latter phase leading to a <101>∥T preferential orientation (**Fig. 6**). On the other hand, ε forms with a main <0001>∥T and a secondary component close to <2-1-10>. This agrees with the two distinct variants of this phase reported to form within prior γ grains [54]. In stage 3 ε deforms by slip as represented by the constant values of the {101}ε lattice strain (**Fig. 4b**) as well as by the shift and the intensity decrease of the pole close to <2-1-10> during this period (**Fig. 6b** and **c**).

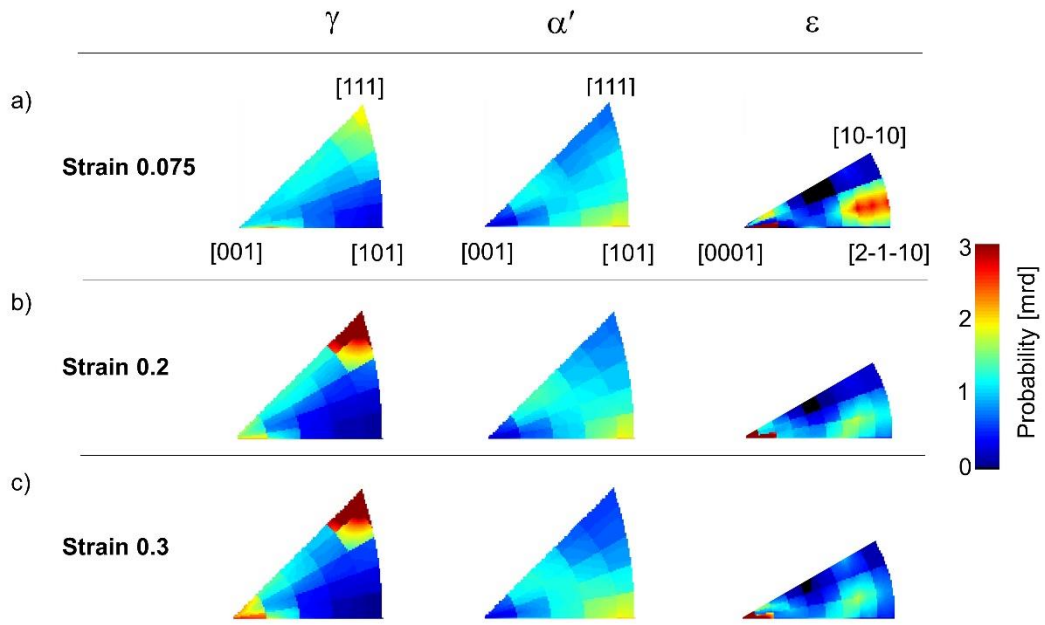

Fig. 6. Inverse pole figures in the tensile direction form the studied bulk alloy obtained using in situ HEXRD showing the texture evolution at the representative strains **a)** 0.075, **b)** 0.2, **c)** 0.3.

3.2. Microstructure analysis

The textures obtained by HEXRD for the maximum applied strain correlate well with those obtained by EBSD for all three phases after tensile deformation (see **Fig. 6c** and **Fig. 7c**, respectively). For the latter investigations, **Fig. 7a** shows a low magnification phase map where regions of γ and α′ can be observed in red and blue, respectively. Also, the presence of ε is identified within shear bands of γ grains (see arrows in **Fig. 7b**).

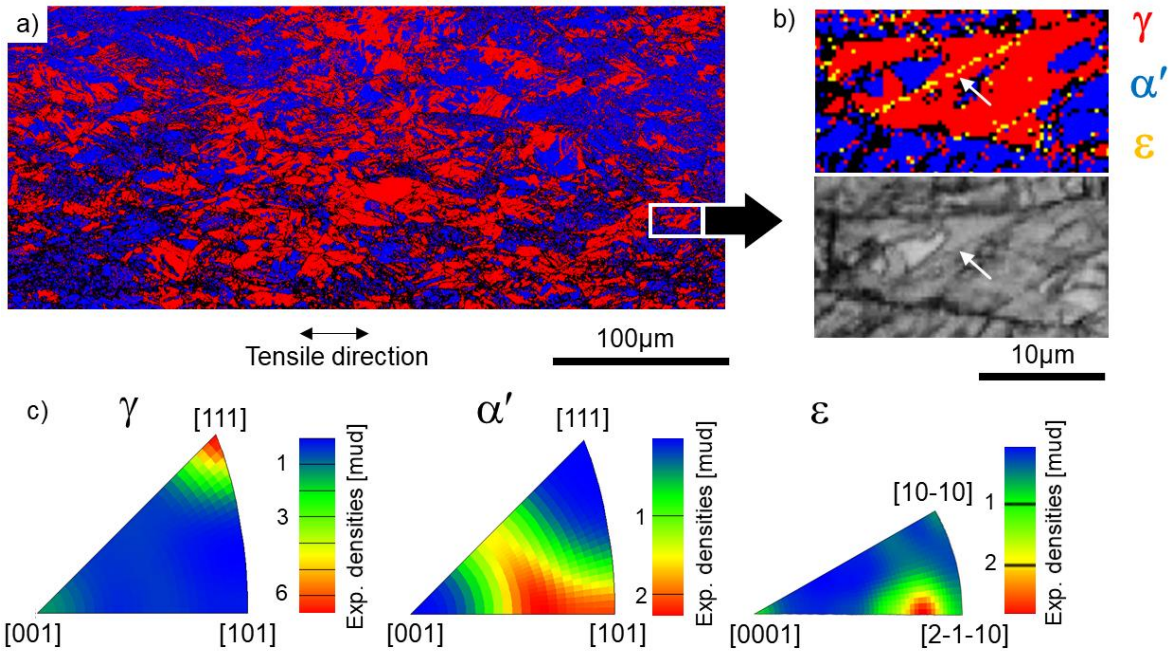

Fig. 7. EBSD of the studied 301LN alloy after tensile deformation up to strain 0.3: **a)** phase map, **b)** phase and band contrast maps of the selected region in a), and **c)** inverse pole figures obtained in the tensile direction from the entire investigated region (540×375 μm^2).

Fig. 8 shows EBSD analysis from two local regions of the 301LN steel after tensile deformation up to strain 0.3. The location of these regions is described in Fig. S1 of

supplementary material. They show two prior γ grains partially transformed into α′ (see **Fig. 8a1**, **a2** and **Fig. 8b1**, **b2**). Fig. **8a3** and **a4** are complementary IPF maps of γ and α′ for one region, showing that <101>α′ ∥ T orientations (in green) can form within <001>γ ∥ T oriented grains (in red). **Fig. 8c** shows that the orientation relationship (OR) given by the pole figure obtained from this region is {001}γ ∥ {101}α′, which can satisfy a OR for the Pitsch pathway {001}γ ∥ {-101}α′ [14, 55]. In the second investigated area, **Fig. 8b3** and **b4** show that <101>α′ ∥T martensite orientations (in green) can also form within <111>γ∥T oriented grains. The associated pole figure points to a OR {111}γ ∥{101}α′ which can be related to the Nishiyama–Wassermann (NW) or Kurdjumov and Sachs (KS) ORs {111}γ ∥ {110}α′. The latter is usually identified in austenitic steels [14, 55]. Previous investigations with a 304 austenitic stainless steel associated the presence of a NW OR with a direct γ → α′ transformation path [55], while the existence of KS and Pitsch ORs derived from the γ → ε → α′ path identified at lower strains. In relation to this, the dominant <111>γ ∥ <101>α′ ∥ T obtained by HEXRD in the present study for the bulk material (**Fig. 6**) supports a major contribution of a direct path not involving the Pitsch OR owing to the weaker <001>γ ∥ T pole observed. The local ORs detected by EBSD in **Fig. 8** allow establishing a relation between texture and γ–α′ transformation and are consistent with the macrotexture evolution of γ and α′ presented in **Fig. 6**. In addition, the dominant <0001>ε ∥ T poles (**Fig. 6**) reflect a Shoji–Nishiyama (SN) {111}γ ∥{0001}ε OR well known to occur in austenitic steels [54].

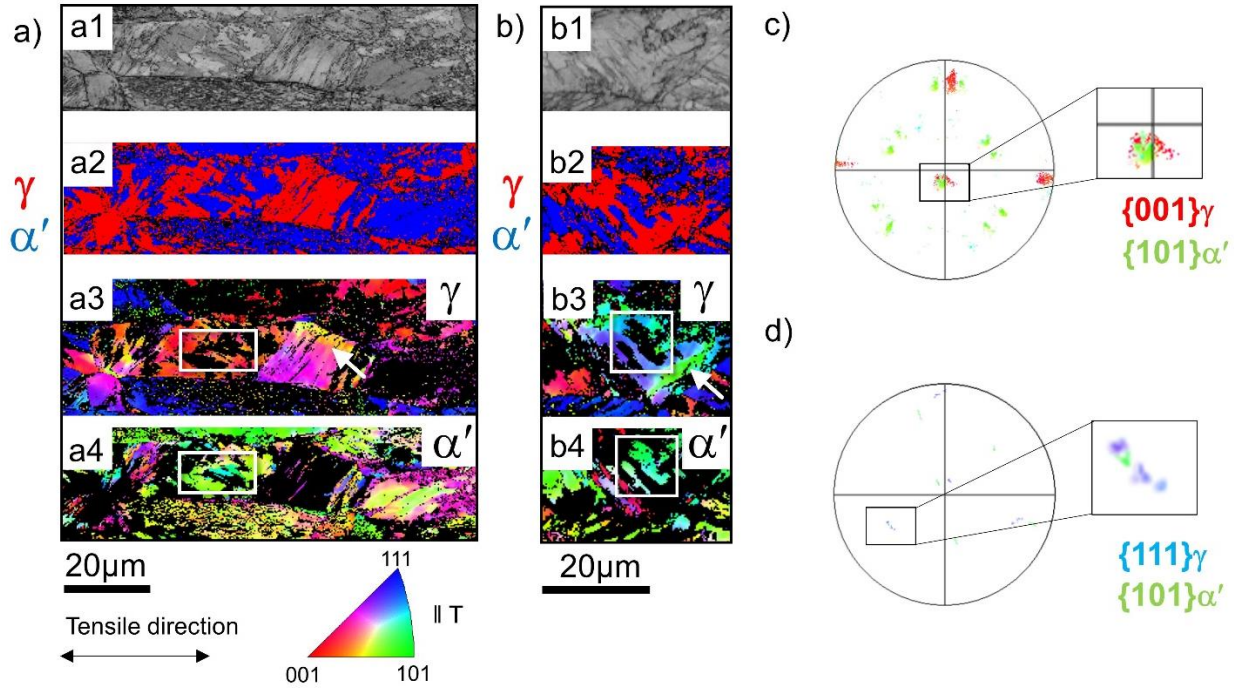

Fig. 8. EBSD of the 301LN alloy after uniaxial tension up to strain 0.3 obtained from two different local regions described in Fig. S1 of supplementary material, **a)** and **b)**: a1, b1) band contrast images, corresponding a2, b2) phase maps, and orientation (IPF) maps of a3, b3) γ and a4, b4) α′. Pole figures for **c)** {001}γ, {101}α′ and **d)** {111}γ, {101}α′ obtained from the insets pointed in a3, a4) and b3, b4), respectively.

During RT mechanical loading, the strain-induced martensitic phase transformation takes place via the formation of deformation bands [5]. These are band-like regions that compared to the surrounding material present a deviating strain state and a frequent orientation variation. They are a prominent deformation mechanism in low-SFE austenitic steels and can form as a consequence of dislocation glide, stacking faults formation or micro twinning [5]. α′ and ε formation have been reported to occur within deformation bands [5, 14]. The latter initiate in grains related to a high Schmid factor; those well-oriented for the activation of slip on {111}γ planes. Increasing plastic strain

increases the number of deformation bands, their thickness, as well as the number of grains containing deformation bands, since slip can then be activated in grains with a lower Schmid factor. In the present work, the important role of slip in triggering α′ formation is revealed by the sudden increase of microstrain (**Fig. 4c**) as well as by the formation of texture poles and grain rotation (**Fig. 5**). These effects take place at the onset of martensite transformation (strain 0.075). In addition, the emergence of subgrains in **Fig. 5b** reflects the progressive fragmentation of prior γ grains during deformation. The generation of deformation bands as precursors of α′ formation is expected to contribute to this effect. In addition, stress partition and the formation of α′ within deformation bands, i.e. within regions with a deviating strain with respect to the γ matrix, may explain the compressive lattice strain observed during transformation for {220}α′ (**Fig. 4b**). Local tensile and compressive stresses in the opposite sides of (111) slip bands have been reported for stainless steel [56].

It is typically documented that shear-band intersections constitute strain-induced nucleation sites of α′ in metastable austenitic steels. These shear bands can be in the form of ε, mechanical twins, stacking-fault bundles and planar slip bands [18, 57]. Further works reported for a 304 stainless steel the nucleation of both ε/α′ on a banded structure of {111}γ dislocation bands [57]. Also, the direct nucleation of α′ along slip lines has been pointed to occur in stainless steel via a γ → slip and band → α′ sequence [14] where α′ gradually coalesces with further deformation. Here, the observed transformation strains (0.076-0.11) are comparable to the onset of α′ observed in the present work (0.075). On the other hand, the γ → ε → α′ path was reported active at lower deformation. The direct path (γ → α′) is also supported by investigations based

on texture analysis which concluded that a two-stage transformation ($\gamma \rightarrow \varepsilon \rightarrow \alpha'$) is not required [16].

On the basis of our investigations, the kinetics described by **Fig. 4a** does not show a $\varepsilon \rightarrow \alpha'$ transformation given by the complementary evolution of phase volume fractions. Thus, its role as an intermediate or transition phase is not seen in the real-time evolution of the bulk material behaviour. Instead, during uniaxial tension, these dominant transformations are observed: $\gamma \rightarrow \varepsilon$ (stage 2) and $\gamma \rightarrow \alpha'$ (stage 3).

Fig. 9a provides an overview of the plastically deformed γ grains on the sample's surface after tensile deformation up to strain 0.3. The creation of deformation bands in primary and secondary slip systems is associated with pronounced surface reliefs (see high magnification observations in **Fig. 9b**). The latter effect is caused by deformation bands along different slip systems and due to the volume dilation accompanying the α' formation [5]. **Fig. 9c** shows a general view of the cross-section obtained from the central part of the tensile specimen prepared by FIB. In the magnified **Fig. 9d**, the white and dark grey contrasts denote that, as a consequence of slip and α' formation, the microstructure becomes significantly fragmented after tensile loading. As pointed by arrows in **Fig. 8a3** and **b3**, the former mechanism causes large misorientation spreads within γ. Also, the fragmentation of γ grains is pointed in **Fig. 5b** and is reflected in the reduction of the crystallite size (see stage 3 in **Fig. 4c**).

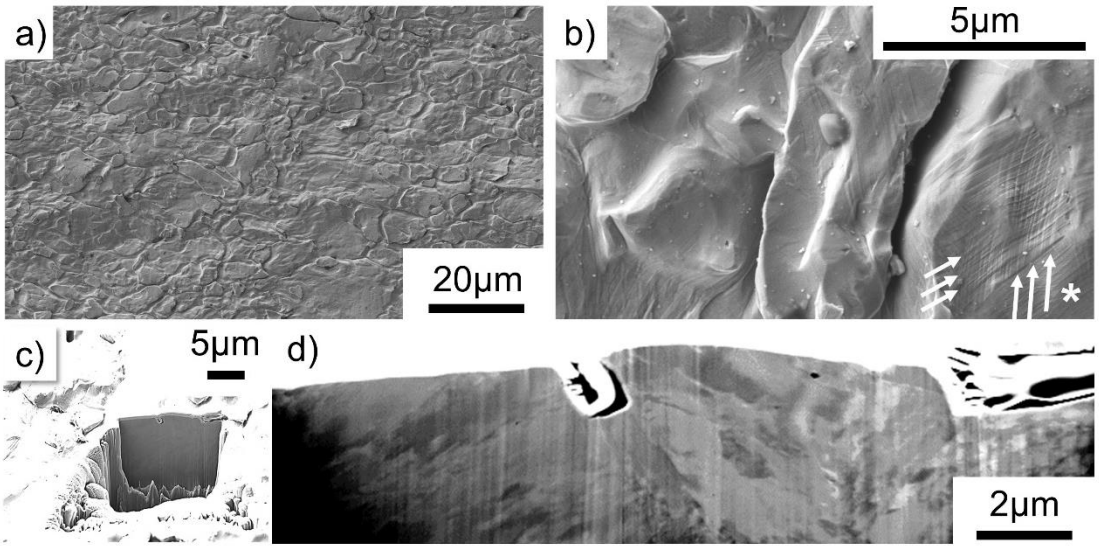

Fig. 9. SEM micrographs of the 301LN alloy obtained from the central region of the tensile sample after tensile deformation up to strain 0.3. **a)** General view of deformed grains on the sample's surface and **b)** detail at higher magnification. **c)** Overview of the sample's cross-section beneath the surface prepared by FIB and **d)** its corresponding microstructure.

Fig. 10 shows TKD analysis of thin-foils prepared by FIB from a selected region of the cross-section depicted in **Fig. 9c**. Both γ and α′ can be distinguished in the phase map of **Fig. 10b**. In **Fig. 10a**, γ appears within a band-like pattern indicating fragmentation by shear band formation while α′ presents in-grain orientation gradients suggesting the presence of subgrains. This is in accordance with the local misorientations provided by the Kernel average misorientation (KAM) map showing maximum values along the grain and cell boundaries of α′ (**Fig. 10c**). Compared to this phase, γ appears highly deformed in this figure. The KAM maps serve as a measure of the deformation-induced local orientation gradients inside these grains. The colour maps of **Fig. 10d** and e show the GNDs distribution. Here, the maximum density of GNDs is mainly located along the

interfaces such as grain boundaries and phase boundaries since the applied stress during tensile testing is higher in these regions [58]. High dislocation densities (in white) are also visible along the subgain boundaries of α′ (**Fig. 10e**).

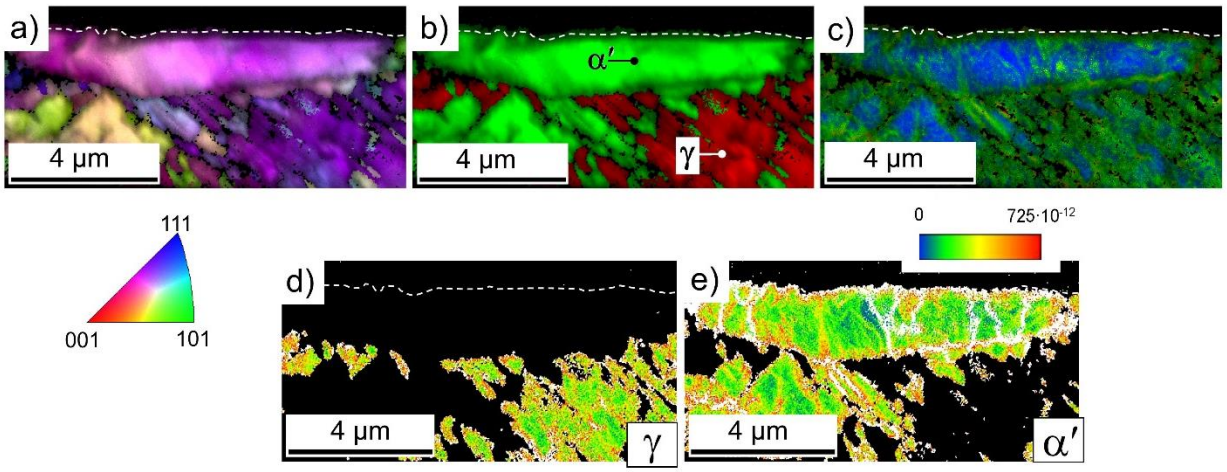

Fig. 10. TKD maps of a thin-foil extracted from the cross-section presented in Fig. 9: **a)** orientation (IPF), **b)** phases, **c)** Kernel average misorientation (KAM) and geometrically necessary dislocations (GND) for **d)** γ and **e)** α′. The sample's surface is indicated by dashed lines.

4. Conclusions

In this study, in situ high-energy synchrotron X-ray diffraction is employed during tensile testing of a metastable austenitic stainless steel 301LN to investigate the deformation kinetics related to the martensitic transformation. The following conclusions are deduced from this work:

- The following stages are identified during deformation:
    1) Stage 1 (strain 0-0.008): the elastic regime results in a linear increase of lattice strains.

2) Stage 2 (strain 0.008-0.075): deformation takes place via the formation of stacking faults and ε. The former is related to the mechanism of ε transformation and is observed as a significant decrease of the crystallite size. The volume fraction evolution of ε presents an asymptotic trend similar to that obtained for the shear-bands, indicating their interrelated formation mechanism.
3) Stage 3 (strain 0.075-0.3): formation of α′ and slip lead to a linear increase of the strain hardening rate. The γ → α′ transformation is triggered by a general activation of slip at its onset. This is indicated by a sudden increase of the microstrain and the initiation of texture poles, grain rotation and subgrain formation in γ.

- The dominant ⟨111⟩∥T (tensile direction) and weaker ⟨100⟩∥T preferential orientations develop in γ during deformation. The former starting to be visible at the onset of slip and α′ formation (strain 0.075), while the latter at higher strain between 0.2–0.3. α′ forms with <101>∥T and this orientation is observed within <111>∥T and <001>∥T grains of γ.
- The following dominant transformations are observed during tensile deformation in stages 2 and 3, respectively: γ → ε and γ → α′. These findings shed light on the role of ε during α′ transformation. They support a major contribution of a direct γ → α′ since no two-stage transformation γ → ε → α′ involving ε → α′ is observed from the bulk analysis obtained.
- The creation of deformation bands in primary and secondary slip systems is associated with pronounced surface reliefs. If these are precursors of α′

formation presenting a deviating strain with respect to the γ matrix, such effect together with stress partition may explain the compressive {220}α′ lattice strain observed in the tensile direction during the transformation.

- The in-grain orientation gradients associated with the formation of geometrically necessary dislocations (GND) and cells in α′ point out to deformation by slip in this phase.

Acknowledgements

The authors would like to thank Outokumpu for supplying the investigated material. The authors are also grateful to the Direcció General de Recerca del Comissionat per a Universitats i Recerca de la Generalitat de Catalunya for recognizing CIEFMA as a consolidated Research Group (2017SGR933). The Deutsches Elektronen-Synchrotron (DESY) is acknowledged for the provision of synchrotron radiation facilities in the framework of proposal I-20191042. Finally, J.J. Roa acknowledges the Serra Húnter programme of the Generalitat de Catalunya for its financial support.

References

[1] Y.H. Kim, K.Y. Kim, Y.D. Lee, Nitrogen-alloyed metastable austenitic stainless steel for automotive structural applications, Mater. Manufact. Proc. 19 (2004) 51-59.

[2] K.H. Lo, C.H. Shek, J.K.L. Lai. Recent developments in stainless steels. Mat. Sci. Eng. R. Report. 65 (2009) 39-104.

[3] V. Zackay, E.R. Parker, D. Fahr, R. Busch. The enhancement of ductility in high-strength steels, Trans. ASM. 60 (1967) 252.

[4] R. Petrov, L. Kestens, A. Wasilkowaska, Y. Houbaert, Microstructure and texture of a lightly deformed TRIP-assisted steel characterized by means of the EBSD technique, Mater. Sci. Eng. A. 447 (2007) 285-297.

[5] A. Weidner, Deformation Processes in TRIP/TWIP Steels, first ed., Springer, Cham, 2020.

[6] D.A. Porter, K.E. Easterling, Phase transformations in metals and alloys, second ed., Chapman & Hall, London, 1993.

[7] H. Berns, W. Theisen, Ferrous materials, Springer, Berlin Heidelberg, 2008.

[8] H.F.G. de Abreu, M.J.G. da Silva, L.F.G. Herculano, H. Bhadeshia, Texture analysis of deformation induced martensite in an AISI 301L stainless steel: microtexture and macrotexture aspects, Mater. Res. 12 (2009) 291-297.

[9] A. di Schino, M. Barteri, J.M. Kenny, Development of ultra fine grain structure by martensitic reversion in stainless steel, J. Mat. Sci. Lett. 21 (2002) 751-753.

[10] P.L. Mangonon, G. Thomas, The martensite phases in 304 stainless steel, Metall. Trans. 1 (1970) 1577-1586.

[11] V. Seetharaman, P. Krishman, Influence of the martensitic transformation on the deformation behavior an AISI 316 stainless steel at low temperatures, J. Mater. Sci. 16 (1981) 523-530.

[12] C. Herrera, D. Ponge, D. Raabe, Design of a novel Mn-based 1 GPa duplex stainless TRIP steel with 60% ductility by a reduction of austenite stability, Acta Mater. 59 (2011) 4653-4664.

[13] N. Li, Y.D. Wang, W.J. Liu, Z.N. An, J.P. Liu, R. Su, J. Li, P.K. Liaw, In situ X-ray microdiffraction study of deformation-induced phase transformation in 304 austenitic stainless Steel, Acta Mater. 64 (2014) 12-23.

[14] J.L. Wang, M.H. Huang, X.H. Xi, C.C. Wang, W. Xu, Characteristics of nucleation and transformation sequence in deformation-induced martensitic transformation, Mater. Charac. 163 (2020) 110234.

[15] G. Nolze, Characterization of the fcc/bcc orientation relationship by EBSD using pole figures and variants. Z. Metallkd. 95 (2004) 744-755.

[16] S. Kundu, H.K.D.H. Bhadeshia, Crystallographic texture and intervening transformations, Scr. Mater. 57 (2007) 869–872.

[17] G.B. Olson, M. Cohen, A mechanism for the strain-induced nucleation of martensitic transformations, J. Less-Common Met. 28 (1972) 107-118.

[18] G.B. Olson, Effects of stress and deformation on martensite formation, Encyclopedia of materials: science and technology (2002) 2381-2384.

[19] T.H. Ahn, C.S. Oh, D.H. Kim, K.H. Oh, H. Bei, E.P. George, H.N. Han, Investigation of strain-induced martensitic transformation in metastable austenite using nanoindentation, Scr. Mater. 63 (2010) 540-543.

[20] R.D.K. Misra, P. Venkatsurya, K.M. Wu, L.P. Karjalainen, Ultrahigh strength martensite-austenite dual-phase steels with ultrafine structure: the response to indentation experiments, Mater. Sci. Eng. A. 560 (2013) 693-699.

[21] A. Das, S. Sivaprasad, P.C. Chakraborti, S. Tarafder, Morphologies and characteristics of deformation induced martensite during low cyclic fatigue behaviour of austenitic stainless steel, Mater. Sci. Eng. A. 528 (2011) 7909-7914.

[22] I. Sapezanskaia, J.J. Roa, G. Fargas, M. Turon-Viñas, T. Trifonov, R.K, Njiwa, A. Redjaïmia, A. Mateo, Deformation mechanisms induced by nanoindentation tests on a metastable austenitic stainless steel: a FIB/SIM investigation, Mater. Charac. 131 (2017) 253-260.

[23] L. Zhao, N.M. van der Pers, J. Sietsma, S. van der Zwaag, In situ X-ray diffraction measurements of deformation-induced austenite to martensite transformation in a multiphase TRIP steel, Mater. Sci. Forum. 379 (2005) 500-501.

[24] E. Jimenez-Melero, N.H. van Dijk, L. Zhao, J. Sietsma, S.E. Offerman, J.P. Wright, S. van der Zwaag, Martensitic transformation of individual grains in low-alloyed TRIP steels. Scr. Mater. 56 (2007) 421-424.

[25] P. Hedström, U. Lienert, J. Almer, M. Odén, Elastic strain evolution and ε-martensite formation in individual austenite grains during in situ loading of a metastable stainless steel. Mater. Lett. 62 (2008) 338-340.

[26] Y. Tian, U. Lienert, A. Borgenstam, T. Fischer, P. Hedström, Martensite formation during incremental cooling of Fe-Cr-Ni alloys: an in-situ bulk X-ray study of the grain-averaged and single-grain behavior, Scr. Mater. 136 (2017) 124-127.

[27] C. Ullrich, S. Martin, C. Schmpf, A. Stark, N. Schell, D. Rafaja, Deformation mechanisms in metastable austenitic TRIP/TWIP steels under compressive load studied by in-situ synchrotron radiation diffraction, Adv. Eng. Mater. 21 (2019) 1801101.

[28] P. Barriobero-Vila, J. Gussone, K. Kelm, J. Haubrich, A. Stark, N. Schell, G. Requena, An in situ investigation of the deformation mechanisms in a β-quenched Ti-5Al-5V-5Mo-3Cr alloy, Mater. Sci. Eng. A 717 (2018) 134-143.

[29] P. Barriobero-Vila, K. Artzt, A. Stark, N. Schell, M. Siggel, J. Gussone, J. Kleinert, W. Kitsche, G. Requena, Mapping the geometry of Ti-6Al-4V: from martensite decomposition to localized spheroidization during selective laser melting, Scr. Mater. 182 (2020) 48-52.

[30] E. Pereloma, D. V. Edmonds, Phase transformations in steel, volume 2: Diffusionless transformations, high strength steels, modelling and advanced analytical techniques, first ed., Woodhead Publishing, 2012.

[31] B. Fu, W.Y. Yang, Y. D. Wang, L.F. Li, Z.Q. Sun, Y. Ren, Micromechanical behavior of TRIP-assisted multiphase steels studied with in situ high-energy X-ray diffraction, Acta Materialia 76 (2014) 342–354.

[32] N. Jia, Z. H. Cong, X. Sun, S. Cheng, Z. H. Nie, Y. Ren, P. K. Liaw, Y. D. Wang, An in situ high-energy X-ray diffraction study of micromechanical behavior of multiple phases in advanced high-strength steels, Acta Mater. 57 (2009) 3965–3977.

[33] Y. Tian, S. Lin, J. Y. P. Ko, U. Lienert, A. Borgenstam, P. Hedström, Micromechanics and microstructure evolution during in situ uniaxial tensile loading of TRIP-assisted duplex stainless steels, Mater. Sci. Eng. A 734 (2018) 281–290.

[34] J.J. Roa, G. Fargas, E. Jiménez-Piqué, A. Mateo, Deformation of polycrystalline TRIP stainless steel micropillars, Mater. Sci. Eng. A. 647 (2015) 51-57.

[35] N. Schell, A. King, F. Beckmann, T. Fischer, M. Müller, A. Schreyer, The high energy materials Beamline (HEMS) at PETRA III, Mater. Sci. Forum 772 (2014) 57–61.

[36] P. Staron, T. Fischer, T. Lippmann, A. Stark, S. Daneshpour, D. Schnubel, E. Uhlmann, R. Gerstenberger, B. Camin, W. Reimers, E. Eidenberger, H. Clemens, N.

Huber, A. Schreyer, In situ experiments with synchrotron high-energy X-rays and neutrons, Adv. Eng. Mater. 13 (2011) 658–663.

[37] M.D. Abramoff, P.J. Magalhaes, S.J. Ram, Image processing with imageJ, Biophoton. Int. 11 (2004) 36–41.

[38] L. Lutterotti, S. Matthies, H.R. Wenk, A.J. Schultz, J. Richardson, Combined textura and structure analysis of deformed limestone from time-of-flight neutron diffraction spectra, J. Appl. Phys. 81 (1997) 594–600.

[39] B. Warren, X-Ray Diffraction, first ed., Dover Publications, New York, 1990.

[40] N. C. Popa, The (hkl) dependence of diffraction-line broadening caused by strain and size for all Laue groups in Rietveld Refinement, J. Appl. Cryst. 31 (1998) 176–180.

[41] G.B. Olson, M. Cohen, Kinetics of the strain-induced martensitic nucleation, Metall. Trans. A 6 (1975) 791-795.

[42] J. Ayache, L. Beaunier, J. Boumendil, G. Ehret, D. Laub, Sample preparation handbook for transmission electron microscopy, first ed., Springer, New York, 2007.

[43] D.P. Field, P.B. Trivedi, S.I. Wright, M. Kumar, Analysis of local orientation gradients in deformed single crystals, Ultramicroscopy 103 (2005) 33-39.

[44] C.J. Guntner, R.P. Reed, The effect of experimental variables including the martensitic transformation on the low-temperature mechanical properties of austenitic stainless steels, Trans. Am. Soc. Met. 55 (1962) 339-419.

[45] J. Talonen, H. Hänninen, Formation of shear bandsand strain-induced martensite during plastic deformation of metastable austenitic stainless steels, Acta Mater. 55 (2007) 6108–6118.

[46] P. Hedström, U. Lienert, J. Almer, M. Odén, Stepwise transformation behavior of the strain-induced martensitic transformation in a metastable stainless Steel, Scr. Mater. 56 (2007) 213-216.

[47] R.M. Christensen, Observations on the definition of yield stress, Acta Mech. 196 (2008) 239–244.

[48] J. Johansson, M. Odén, H. Zhang, Evolution of the residual stress state in a duplex stainless steel during loading, Acta Mater. 47 (1999) 2669-2684.

[49] S. Li, T. Wang, Q. Tan. R. Li, Y. Wang, X. Wang, Y. Ren, Y. Wang, A brittle fracture mechanism in thermally aged duplex stainless steels revealed by in situ high-energy X-ray diffraction, Mater. Sci. Eng. A 739 (2019) 264-271.

[50] C. Ullrich, R. Eckner, L. Krüger, S. Martin, V. Klemm, D. Rafaja, Interplay of microstructure defects in austenitic steel with medium stacking fault energy, Mater. Sci. Eng. A 649 (2016) 390-399.

[51] S.D. Yadav, S. Kalácska, M. Dománková, D.C. Yubero, R. Resel, I. Groma, C. Beal, B. Sonderegger, C. Sommitsch, C. Poletti, Evolution of the substructure of a novel 12% Cr steel under creep conditions, Mater. Charac. 115 (2016) 23-31.

[52] K.D. Liss, K. Yan, Thermo-mechanical processing in a synchrotron beam, Mater. Sci. Eng. A 528 (2010) 11-27.

[53] B.C. De Cooman, Y. Estrin, S.K. Kim, Twinning-induced plasticity (TWIP) steels, Acta Mater. 142 (2018) 283-362.

[54] M. Eskandari, A. Zarei-Hanzaki, M.A. Mohtadi-Bonab, Y. Onuki, R. Basu, A. Asghari, J.A. Szpunar, Grain-orientation-dependent of γ-ε-α′ transformation and

twinning in a super-high-strength, high ductility austenitic Mn-steel, Mater. Sci. Eng. A 674 (2016) 514-528.

[55] Y. He, K. Wang, K. Shin, Correlation of orientation relationships and strain-induced martensitic transformation sequences in a gradient austenitic stainless Steel, J. Mater. Sci. 56 (2021) 4858-4870.

[56] R. Lia, Q. Xiea, Y.D. Wang, W. Liu, M. Wang, G. Wu, X. Li, M. Zhang, Z. Lu, C. Geng, T. Zhu, Unraveling submicron-scale mechanical heterogeneity by three-dimensional X-ray microdiffraction, PNAS 115 (2918) 483-488.

[57] N. Gey, B. Petit, M. Humbert, Electron backscattered diffraction study of ε/α′ martensitic variants induced by plastic deformation in 304 stainless steel, Metall. Mater. Trans. A 36 (2005) 3291-3299.

[58] I.R.S. Filho, A. Dutta, D.R.A. Junior, W. Lu, M.J.R. Sandim , D. Ponge, H.R.Z. Sandim, D. Raabe, The impact of grain-scale strain localization on strain hardening of a high-Mn steel: real-time tracking of the transition from the γ→ε→α′ transformation to twinning, Acta Mater. 197 (2020) 123-136.